Harmonic Stability Assessment for Multiparalleled, Grid-Connected Inverters

Changwoo Yoon, *Student Member, IEEE*, Haofeng Bai, *Student Member, IEEE*, Remus Narcis Beres, *Student Member, IEEE*, Xiongfei Wang, *Member, IEEE*, Claus Leth Bak, *Senior Member, IEEE*, and Frede Blaabjerg, *Fellow, IEEE*

***Abstract*—This paper investigates the harmonic interactions of current controllers in multiparalleled grid-connected inverters. Potential harmonic instability phenomenon, which features oscillations above the fundamental frequency, is evaluated by the impedance-based stability criterion. The possible reasons of the destabilized inverter with different types of grid impedances are explained by the passivity-based analysis and impedance-based stability criterion. Thereafter, case studies are provided, which shows how the nonpassive grid connected inverters interact with the varying grid impedance due to load changes or by the new connections of other grid-connected inverters. Time domain simulations in the PSCAD/EMTDC environment and experimental results show the corresponding harmonic interaction problems may exist in nowadays power system and the impedance-based stability analysis can be an effective tool to assess those problems.**

***Index Terms*—Impedance based stability criterion, harmonic stability, distribution generation, inverter output impedance, grid impedance, passivity.**

I. Introduction

In these days, renewable energy sources have been developed to meet the expected future electric energy consumption and they are now widely commercialized. However, unidentified problems arise with larger numbers of power electronics based systems employed in the existing AC distribution network. In a Dutch distribution network with a high penetration of Photovoltaic (PV) generation, it has been reported that occasionally the PV inverters were switched off unexpectedly [1]. Even each of the PV inverter is designed individually stable according to grid connection standards [2], the power quality at the Point of Common Coupling (PCC) may still exceed the requirement [3]. Recent research shows that impedance interactions between the multiple inverters may cause resonance amplification and the consequent harmonic instability [2]. To address and mitigate these undesirable phenomena, the Impedance-Based Stability Criterion (IBSC) is emerging as an effective analysis tool [4], [5]. The IBSC was originated from the design of input filters for DC-DC converters [4], [6], which was later extended to study the dynamic interactions of the multiple interconnected DC-DC converters. Recently, the IBSC was applied to analyze the interaction problems in AC distribution power systems with multiple inverters [2], [7]. The harmonic instability, which is mainly caused by the interactions of the fast inner current control loops with the output LCL-filter parameters and grid impedance [2], [8] may exhibit resonances in a wide frequency range. Then, it is difficult to find the problematic frequency range, where the harmonic instability exists.

The concept of passivity, which was originated in control engineering, has recently been gaining attention [9]. It was adopted to mitigate harmonic interactions between paralleled inverter units [10]. This concept can deal with a large and complex control system by imposing specific requirements for each individual subsystem to guarantee the overall system stability. It provides a phase angle based design guide-line for all connected sub-systems, e.g. each subsystem should have a phase angle between $[-90°, +90°]$, in order not to be affected by the other subsystems such as transmission or distribution lines, power filters or multi-paralleled inverters nearby [10].

In practice, a short response time of the inverter may be required, which is often achieved with the price of non-passivity. Again, this may result in harmonic instabilities for certain grid conditions. Therefore, in this paper, the IBSC and passivity concept are used to analyze the stability of multi-paralleled inverters under different grid impedances.

The modeling of grid-connected inverter output impedance is presented first. In Section III, the non-passive region of LCL-filtered inverter with the grid current control is presented, given that the inverter is inherently stable despite its control time delay [11]. For the passive grid impedance, the only frequency region which may cause harmonic instability is the non-passive region of the output impedance of the inverter. Therefore, the analysis is focused on the non-passive region together with different types of passive grid impedances and which are presented and analyzed in Section IV by the use of IBSC. Furthermore, sufficient conditions for the stability are revealed. Since the power distribution system may contain multiple inverters, the grid impedance may not be passive at all. It may depend on the operating conditions of the inverters, loads, feeder impedances and it becomes very complex to take all possible cases into account. Therefore, in Section V, time domain simulations in PSCAD/EMTDC environment are performed and validated with numerical computations of the IBSC which check the system stability. Experimental tests are provided to demonstrate the harmonic interactions between paralleled inverters and grid impedance. The results and main findings conclude the present work.

Manuscript received October 26, 2015; revised February 08, 2016; accepted March 07, 2016. Date of publication April 20, 2016; date of current version September 16, 2016. This work was supported by the European Research Council under the European Union's Seventh Framework Program (FP/2007-2013)/ERC Grant [321149-Harmony]. Paper no. TSTE-00884-2015.

The authors are with the Department of Energy Technology, Aalborg University, 9220 Aalborg, Denmark (e-mail: cyo@et.aau.dk).

Color versions of one or more of the figures in this paper are available online at http://ieeexplore.ieee.org.

Digital Object Identifier 10.1109/TSTE.2016.2551737

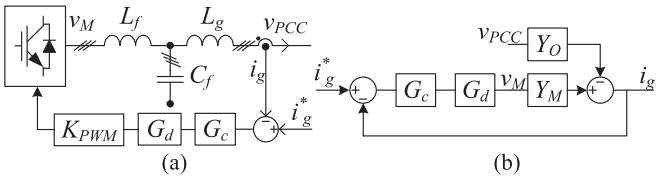

Fig. 1. (a) Single-phase representation of LCL-filtered inverter with grid current control (b) Averaged switching model of the grid inverter.

II. Modeling of Inverter Output Impedance

The single-phase representation of a three-phase grid-connected inverter with grid-current control is illustrated in Fig. 1(a). In order to model the inverter output impedance, the averaged switching model is used as illustrated in Fig. 1(b). In addition to the filter in the control loop, there is a current controller (G_c), a time delay from the computation and pulse width modulation (G_d) [12], [13], and a modulator gain K_{PWM} defined as:

$$G_c(s) = K \tag{1}$$

$$G_d(s) = e^{-1.5T_s s} \tag{2}$$

$$K_{PWM} = 1 \tag{3}$$

The input output relations of the filter from Fig. 1(a) ignoring the parasitic resistances of the passive components can be defined as:

$$Y_O(s) = \left.\frac{-i_g}{v_{PCC}}\right|_{v_M=0} = \frac{s^2C_fL_f+1}{s(s^2C_fL_fL_g+L_f+L_g)} \tag{4}$$

$$Y_M(s) = \left.\frac{i_g}{v_M}\right|_{v_{PCC}=0} = \frac{1}{s(s^2C_fL_fL_g+L_f+L_g)} \tag{5}$$

Finally, the inverter output admittance can be defined as:

$$Y_C(s) = \left.\frac{i_g}{v_{PCC}}\right|_{i_g^*=0} = \frac{Y_O}{1+G_cG_dY_M} = \frac{s^2C_fL_f+1}{s^3C_fL_fL_g+s(L_f+L_g)+Ke^{-1.5T_s\cdot s}} \tag{6}$$

where K is the proportional gain of the current controller; T_s is the sampling time of the inverter in seconds; i_g is the grid current; v_M and v_{PCC} are the modulator and the point of common coupling (PCC) voltages, respectively; L_f and L_g are the converter and grid side inductances of the filter, and C_f is the filter capacitor.

III. Passivity-Based Stability Analysis of the Inverter Output Impedance

A. Concept of Passivity

The concept of passivity originally was mentioned in network theory which dealt with linear networks considering time and energy relation [14]. This defined the passive network, i.e., impedances $Z(s)$, as a necessary and sufficient condition that a linear network is passive if its impedance is a positive real function. More accurate formulation was followed thereafter; that is, $\mathrm{Re}\int_{-\infty}^{t} v^*(\tau)i(\tau)d\tau \geq 0$ for all $t > -\infty$,

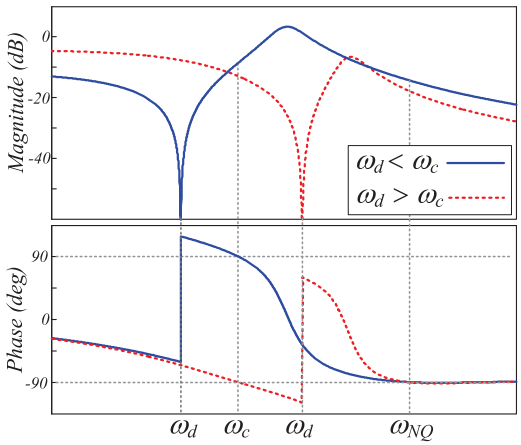

Fig. 2. Inverter output admittance Y_C for two different designs of LCL filter resonance frequency.

where v, i and $*$ are stimulus voltage, output current and complex conjugate respectively [15]. The total energy delivered to the network becomes; $\frac{1}{\pi}\int_0^{+\infty}\mathrm{Re}[Z(j\omega)]\|I(j\omega)\|^2 d\omega$ and it has to be greater than 0, which impose that $\mathrm{Re}[Z(j\omega)] \geq 0$ at each frequency [16]. This criteria guarantees the phase angle of impedance $Z(s)$ to be in a passive range, given by $[-90°, +90°]$. If we assume that our complex impedance network is composed of many sub-systems, then the stability of the system is determined by its impedance relations. Recalling, if there are only passive sub-systems, the maximum phase angle of the interconnected system must be in the $[-180°, +180°]$ which never encircles $(-1, \mathrm{j}0)$ in the Nyquist plot, resulting in a stable system. Therefore, if we put the responsibility on each connected inverter by keeping the common rule of passivity, the entire system can achieve stable operation at all time [17].

B. Pole-Zero Frequencies of Inverter Output Admittance

Fig. 2 shows typical Bode diagrams of grid current controlled inverter with LCL filter and two different possible designs. Both filter designs result in an inverter output admittance, which has notable changes in the magnitude and phase frequency responses. For example, the inverter admittance magnitude has a pronounced dip (anti-resonance) at a frequency ω_d given by:

$$\omega_d = \sqrt{C_fL_f}^{-1} \tag{7}$$

which is derived from the double zeros shown in (6). New terms are defined to confine the area of analysis, therefore the LCL filter resonance frequency ω_{res} and the critical frequency of the inverter ω_c is given by:

$$\omega_{res} = \sqrt{\frac{L_f+L_g}{L_fL_gC_f}} \tag{8}$$

$$\omega_c = \frac{\pi}{3T_s} \tag{9}$$

The critical frequency of the inverter ω_c is one-sixth of the sampling frequency. If $\omega_{res} > \omega_c$ is satisfied, then the inverter does not need resonance damping for its stand-alone stable operation [11]. Lastly, the Nyquist frequency ω_{NQ} is defined as the half of the sampling frequency.

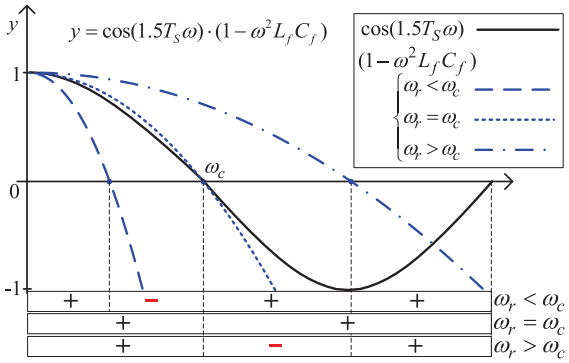

Fig. 3. Non-passive region of grid inverter derived from the numerator of $\Re(Y_C)$.

Likewise, the locations of the anti-resonance frequency ω_d in respect to ω_c, which are $\omega_d > \omega_c$ and $\omega_d < \omega_c$, make two distinctive ways of classifying the non-passive region in Fig. 2. The phases of the two admittances exceed the passive range $[-90°, +90°]$ in the interval of (ω_d, ω_c) or (ω_c, ω_d), respectively, even though the inverter is designed stable as standalone. Due to their inductive dominant characteristics, the phase angle of Y_C starts with 0 degree and ends with -90 degree in both cases. Additionally, the phase angle degradations are introduced by the time delay term G_d until they reach ω_d and where the $180°$ phase jump occurs. Therefore, the time delay and the parallel resonance frequency ω_d are the main reason of passivity violation of the inverter.

C. Non-Passive Range of Inverter Output Admittance

As explained in [17], the passivity violation can be identified by inspecting the existence of the negative real part of the output admittance:

Eq. (10) identifies a factor which determines the sign of the real part of Y_C [18]. Since the denominator is always greater than 0, the only factor which determines the sign is the cosine function (which comes from the time delay G_d) and the anti-resonance term ω_d. In Fig. 3 the plots of each significant term in the numerator of (10), shown at the bottom of the page, and their combined polarities are shown and both determine the non-passive region of the inverter. The cosine term changes its polarity at ω_c and it changes to positive again at the Nyquist frequency ω_{NQ}. The $(1 - \omega^2\, C_f L_f)$ term is drawn for different frequencies of ω_d. There are three different ranges depending on the different values of ω_d. When ω_d is smaller than ω_c, the non-passive region becomes $[\omega_d, \omega_c]$ and when ω_d is larger than ω_c, the non-passive region becomes $[\omega_c, \omega_d]$. Specially, when ω_d is equal to ω_c, the non-passive region disappears [19] and the system becomes stable for all passive network admittance.

The frequency range for harmonic analysis is limited for easy explanation to the Nyquist sampling frequency ω_{NQ}. However, above the Nyquist frequency, there may be issues, which still need to be investigated [20]. Therefore, this paper analyzes the non-passive region of the LCL-filtered grid connected inverter, where the stability may be affected by the passive grid impedances with frequencies up to ω_{NQ}.

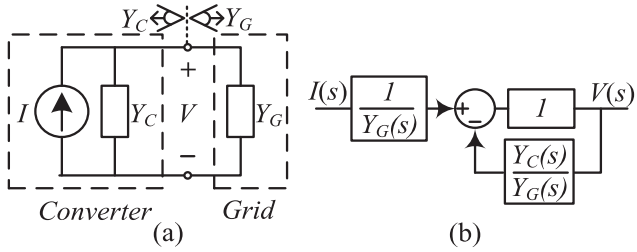

Fig. 4. Small-signal admittance representation of (a) an interconnected system with current source; (b) the minor loop gain representation.

IV. Stability Analysis for Different Grid Impedances

In this section, stability regions of the inverter output admittance Y_C with different grid admittance Y_G are described. By using the graphical interpretation with IBSC, the non-passive region of the inverter can provide the possible forbidden regions of the passive grid admittances. Thus the critical grid admittance and the sufficient grid conditions for stable operation of the inverter can be drawn.

A. Impedance Based Stability Analysis (IBSC)

The IBSC uses terminal impedance/admittance characteristics of the converter output (Y_C) and grid admittances (Y_G) to find out the interconnected system stability as shown in Fig. 4(a). The stability of the interconnected system can be identified by the so called minor loop gain L_M [4] shown in Fig. 4(b) and defined as:

$$L_M = \frac{Y_C}{Y_G} \tag{11}$$

For stability analysis, the magnitude condition $|Y_C| > |Y_G|$ and the negative phase angle crossover condition $(\angle Y_C - \angle Y_G = -\pi \pm 2\pi N)$ should be satisfied.

B. Influence of Pure Inductive Grid Impedance

In order to find the magnitude condition for the pure inductive grid, the admittance magnitude of the non-passive region of the inverter $|Y_C(j\omega)|$ is needed. Since the given grid impedance is passive, the frequency range of concern is limited to the non-passive range of the inverter. The critical frequency ω_c is the reference mark of the non-passive region and where the phase of the inverter crosses its ± 90 degrees. As a result, the magnitude comparison at ω_c becomes the first step to check the stability of the interconnected system.

For the pure inductive grid, the admittance and the critical inductance value of the grid inductance L_G can be calculated

$$\Re\left(Y_C(j\omega)\right) = \frac{K\cos(1.5\,T_s\omega)(1-\omega^2 C_f L_f)}{\left(K\sin(1.5\,T_s\omega) + \omega\left(\omega^2 C_f L_f L_g - L_f - L_g\right)\right)^2 + \left(K\cos(1.5\,T_s\omega)\right)^2} \tag{10}$$

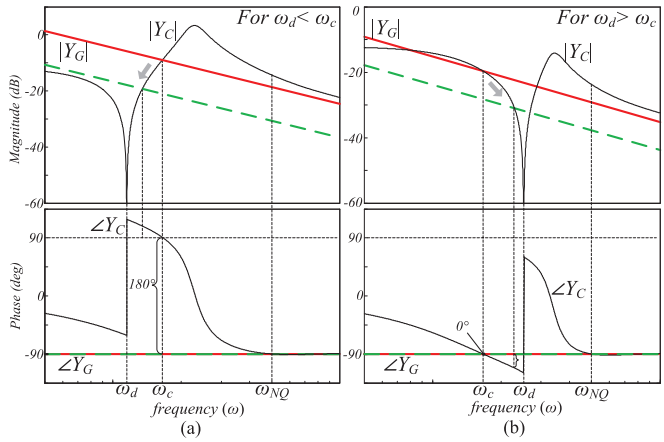

Fig. 5. Stable and unstable region of grid inverter in pure inductive grid case; (a) $\omega_d < \omega_c$, (b) $\omega_d > \omega_c$.

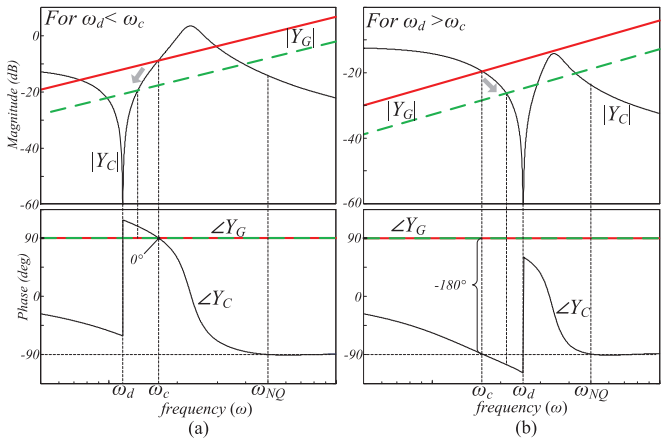

Fig. 6. Stable and unstable region of grid inverter in pure capacitive grid case; (a) $\omega_d < \omega_c$, (b) $\omega_d > \omega_c$.

by equating the grid admittance (12) to the output admittance of the inverter (6) at the critical frequency ω_c as follows:

$$Y_G(j\omega) = \frac{1}{j\omega L_G} \tag{12}$$

When the grid inductance L_G increases, the admittance line $|Y_G|$ (solid line) moves downwards as illustrated with dashed line in Fig. 5. The area for satisfying the magnitude condition $|Y_C| > |Y_G|$ starts to be broadened. Then, the frequency where the negative crossover takes place ($\angle Y_C - \angle Y_G = -\pi \pm 2\pi N$), in this case ω_c, starts to be included in the magnitude inversion region as shown in Fig. 5(a). However, depending on the anti-resonance frequency ω_d, the phase difference of the two admittances can be zero, which is the most stable condition, as shown in Fig. 5(b). It is from the phase angle of pure inductive grid admittance (-90 degree). Therefore, the pure inductive grid can make the system unstable only when $\omega_d < \omega_c$ and L_G larger than in (13), shown at the bottom of the page.

C. Influence of Pure Capacitive Grid Impedance

Similarly, the critical frequency is also analyzed for the capacitive grid which may occur if the inverter is connected with the grid through long underground cables. The stability analysis for variable capacitance C_G works inversely as the L_G in the inductive grid impedance. By the same method as in the pure inductive grid, boundary capacitance value can be found by equating the grid admittance (14) with the output admittance of the inverter Y_C (6) at the critical frequency ω_c:

$$Y_G(j\omega) = j\omega C_G \tag{14}$$

The grid admittance $|Y_G|$ (solid) moves downwards as C_G decrease, and it becomes the dashed line of Fig. 6. Different from the pure inductive grid case, the phase angle of Y_G is fixed to $+90$ degrees, the interconnected system becomes unstable only when $\omega_d > \omega_c$ and C_G is smaller than the boundary value (15), shown at the bottom of the page, as shown in Fig. 6(b).

D. Influence of Resistive- Inductive (RL) Grid Impedance

As it is explained in the previous sections, the inductive grid impedance, just like the normal cables, creates problems for the inverter only with $\omega_d > \omega_c$ as explained in (13). Furthermore, if the grid impedance contains resistive impedance, the system becomes relatively more stable by its resistive damping as shown by:

$$Y_G(j\omega) = \frac{1}{j\omega L_G + R_G} \tag{16}$$

However, a complexity problem appears on managing the equation when the grid impedance contains a resistive value. Rules for judging the unstable region become more complicated and an explicit solution for satisfying the equation is more difficult to be obtained. Therefore, another conservative way of defining the system stability region is necessary to get an analytical solution.

If the magnitude condition $|Y_G(j\omega)| \geq |Y_C(j\omega)|$ is satisfied in the interval $\omega_d < \omega < \omega_c$, then the inverter is always stable. Therefore, the sufficient magnitude condition is derived in (17), shown at the bottom of the next page, and is illustrated in the magnitude plot in Fig. 7. If the magnitude condition (17) is not

$$L_G = \frac{\sqrt{K^2\cos^2(1.5\,T_s\omega_c) + \left(K\sin(1.5\,T_s\omega_c) + \omega_c\left(\omega_c^2 C_f L_f L_g - L_f - L_g\right)\right)^2}}{\omega_c\left|1 - \omega^2 C_f L_f\right|} \tag{13}$$

$$C_G = \frac{\left|1 - \omega^2 C_f L_f\right|}{\omega_c\sqrt{K^2\cos^2(1.5\,T_s\omega_c) + \left(K\sin(1.5\,T_s\omega_c) + \omega_c\left(\omega_c^2 C_f L_f L_g - L_f - L_g\right)\right)^2}} \tag{15}$$

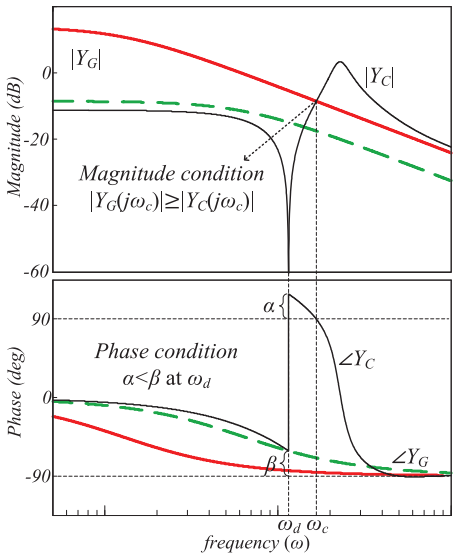

Fig. 7. Sufficient stable condition for grid inverter with RL grid impedance for $\omega_d < \omega_c$.

satisfied, it does not mean that the system is unstable. The system can be stable with large R_G, which can be explained by its resistive damping. Therefore, the additional phase condition has to be applied in order not to create a too conservative condition. A maximum non-passive phase angle, which creates the worst condition of the phase angle difference, is used to define the sufficient conditions in the phase plot illustrated in Fig. 7. The terms α, β are as obtained as follows:

$$\alpha(\omega) = \tan^{-1}\left(\tan\left(\frac{3}{2}T_s\omega\right) + \frac{\omega\left(\omega^2 C_f L_f L_g - (L_f + L_g)\right)}{K\cos(\frac{3}{2}T_s\omega)}\right) \pm \frac{\pi}{2}\Bigg|_{\substack{+)\omega_r<\omega_c \\ -)\omega_r>\omega_c}} \tag{18}$$

$$\beta(\omega) = \tan^{-1}\left(-\frac{L_G}{R_G}\omega\right) + \frac{\pi}{2} \tag{19}$$

The abrupt phase change appears at the frequency ω_d and it becomes the maximum phase shift angle. Eq. (20) shows the condition in which the phase angle of the inverter degrades faster than the phase drop of the grid impedance in the non-passive region. It means that the worst phase condition can be found only by checking the phase difference at ω_d. If both (20) and (21) are satisfied, then the inverter with RL grid impedance is always stable.

$$\frac{9{T_s}^2(L_f + L_g) - \pi^2 L_f L_g C_f}{(3T_s)^3 K} > 1 \tag{20}$$

$$\alpha(\omega_d) \le \beta(\omega_d) \tag{21}$$

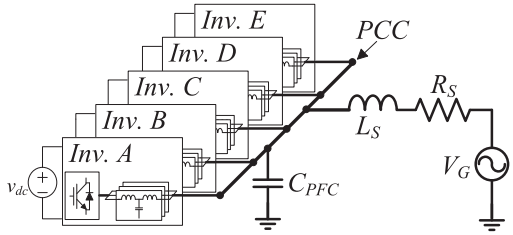

Fig. 8. Single line diagram of three-phase distribution power system with five inverters in parallel.

V. Stability Analysis of Multi-Paralleled Grid Connected Inverters

In power distribution system there are many connected DG units, some of them can be non-passive inherently and they may affect the system stability as well. In this case, the grid impedance seen from one grid inverter cannot be considered as purely passive impedances but is affected by other inverters or non-passive active loads; therefore, they create non-passive grid impedance which is even more difficult to be estimated. Therefore, a parameter sweep method and random case simulations are adopted to check the distribution system stability. Fig. 8 shows an inverter based power distribution system with five paralleled inverters, which is aimed for harmonic stability assessment. All of the inverters are furnished with the passively damped LCL-filters and their power ratings are designed according to the Cigré LV benchmark system [21].

There are two types of case studies: one is the effect of the grid impedance variation and the other one is the possible unstable operating conditions of the paralleled inverters. All cases are investigated by the IBSC, and PSCAD time-domain simulations and experimental tests are used to verify the results.

A. System Description

As shown in Fig. 8, the system contains five different ratings of three-phase Voltage Source Inverters (VSI) in parallel. All are connected to the PCC and are operated in grid connected mode. For simplification, the inverters are supplied from a constant DC voltage source. There is a three-phase capacitor C_{PFC} connected to the PCC in parallel, which might be used for Power Factor Correction (PFC) for an existing load system like Direct-On-Line (DOL) startup motor application. The grid voltage is set as the line to line 400 V rms at 50 Hz. The default value of the PFC capacitor is 12 uF. The grid impedance consists of a 400 uH inductance and a 0.1 Ω resistor, which is series connected. For the PSCAD/EMTDC time-domain simulation, the inverter model with the stationary axis Proportional + Resonant (P + R) controller for the grid side current i_g is used as shown in Fig. 9. All inverters have the same filter structure, which is the Inductor–Capacitor-Inductor (LCL)

$$\frac{1}{\sqrt{L_G^2\omega_c^2 + R_G^2}} \ge \frac{\left|1 - \omega^2 C_f L_f\right|}{\sqrt{K^2\cos^2(1.5\,T_s\omega_c) + \left(K\sin(1.5\,T_s\omega_c) + \omega_c\left(\omega_c^2 C_f L_f L_g - L_f - L_g\right)\right)^2}} \tag{17}$$

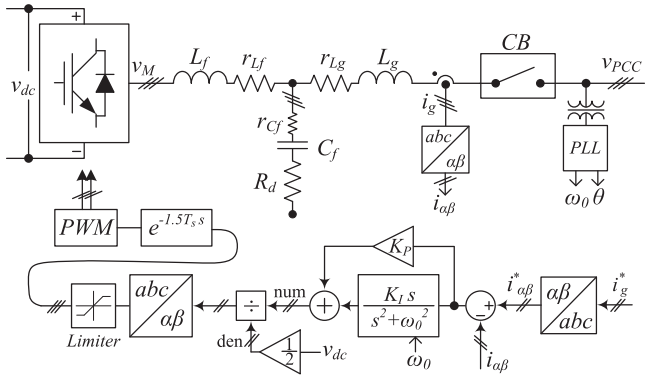

Fig. 9. Grid inverter control diagram for PSCAD implementation.

TABLE I
GRID INVERTER SPECIFICATIONS AND PARAMETERS

		Inverter name				
		Inv. A	Inv. B	Inv. C	Inv. D	Inv. E
Power rating [kVA]		35	25	3	4	5.5
Base Frequency, f_0 [Hz]		50				
Switching and sampling Frequency, f_s [kHz]		10		16		10
DC-link voltage, v_{dc} [V]		750				
Harmonic regulations of LCL filters		IEEE519-1992	1992	1992	1992	2014[a]
Filter values	*Lf [mH]*	0.87	1.2	5.1	3.8	0.8
	Cf [uF] / Rd [Ω]	22/0.2	15/1.4	2/7	3/4.2	15/0.9
	Lg [mH]	0.22	0.3	1.7	1.3	0.2
Parasitics Values	*rLf [mΩ]*	11.4	15.7	66.8	49.7	10
	rCf [mΩ]	7.5	11	21.5	14.5	11
	rLg [mΩ]	2.9	3.9	22.3	17	2.5
Controller Gain	*KP*	5.6	8.05	28.8	16.6	6.5
	KI	1000	1000	1500	1500	1000

[a] : refer to [3]

filter. The LCL filters are designed under the consideration of the IEEE-519 [3] harmonic recommendation. Also, there are parasitic components such as the Equivalent Series Resistance (ESR) for each of the filter components. Further, the passive-damping resistor R_d is placed in series with capacitor C_f for stabilizing the inverter stand-alone. The inverter model uses the Sinusoidal Pulse Width Modulation (SPWM) method and the sampling delay is represented as an exponential delay function. The filter parameters and controller gains are summarized in Table I. The admittance model of the inverter for the IBSC can be derived as in the Chapter II, except the parasitic resistances of the LCL-filter and P + R current controller which are considered in this case as depicted in Fig. 9. Therefore, the necessary minor loop gains for the IBSC are found.

B. Case Studies of Varying Grid Impedance

There are five inverters in parallel with a capacitor and the RL grid impedance. Therefore, the source admittance Y_{SG} and the load admittance Y_{LG} can be derived as in (22) and (23), respectively.

$$Y_{SG} = \frac{1}{R_S + sL_S} \tag{22}$$

where R_S is grid resistance and L_S is grid inductance as shown in Fig. 8.

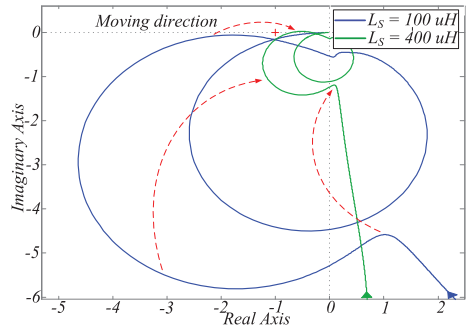

Fig. 10. The Nyquist plots of the minor loop gain T_{MG} with the different grid inductance L_S and its moving trajectory as L_S increases.

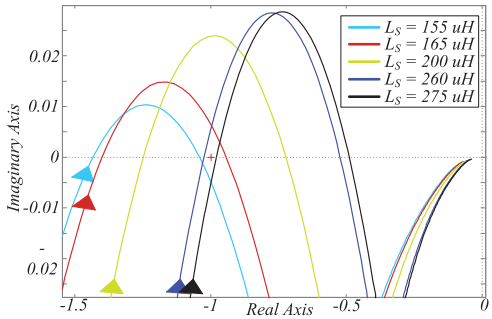

Fig. 11. The Nyquist plots for the marginally stable values of LS.

$$\begin{aligned} Y_{LG} &= Y_{CPFC} + \sum_{X=A}^{E} Y_{CLX} \\ &= sC_{PFC} + Y_{CLA} + Y_{CLB} + Y_{CLC} + Y_{CLD} + Y_{CLE} \end{aligned} \tag{23}$$

where Y_{CPFC} denotes the admittance of capacitor C_{PFC} as shown in Fig. 8.

Finally, the minor loop gain T_{MG} is obtained as follows:

$$T_{MG} = \frac{Y_{SG}}{Y_{LG}} \tag{24}$$

Each variation in Y_{SG} results in different minor loop gains T_{MG} which can further be compared with time-domain simulation results. Variations are made by changing the L_S value from 100 uH to 400 uH and the trajectory is represented as red arrows with dotted lines as shown in Fig. 10. The two diagrams in Fig. 10 are not encircling the $(-1, \text{j}0)$ point, hence the power system with both L_S cases are stable. However, there is a range of grid inductance values which makes the Nyquist plot of T_{MG} to encircle the $(-1, \text{j}0)$ point, as shown in Fig. 11. The accuracy is measured by the value which moves the plot in the vicinity of the $(-1, \text{j}0)$ point. The plot moves from the stable value $(L_S = 155$ uH$)$ and passes the unstable values $(L_S = 165$ uH ~ 260 uH$)$ and becomes stable $(L_S = 275$ uH$)$ again. The parameters used in the simulation are listed in the Table I. Fig. 12 shows the respective PSCAD time-domain simulation results. It matches with the results in Figs. 10 and 11. When the Nyquist plot shows some stable conditions, the respective time domain simulations are not distorted and the output current of the inverter reaches the steady state fast as

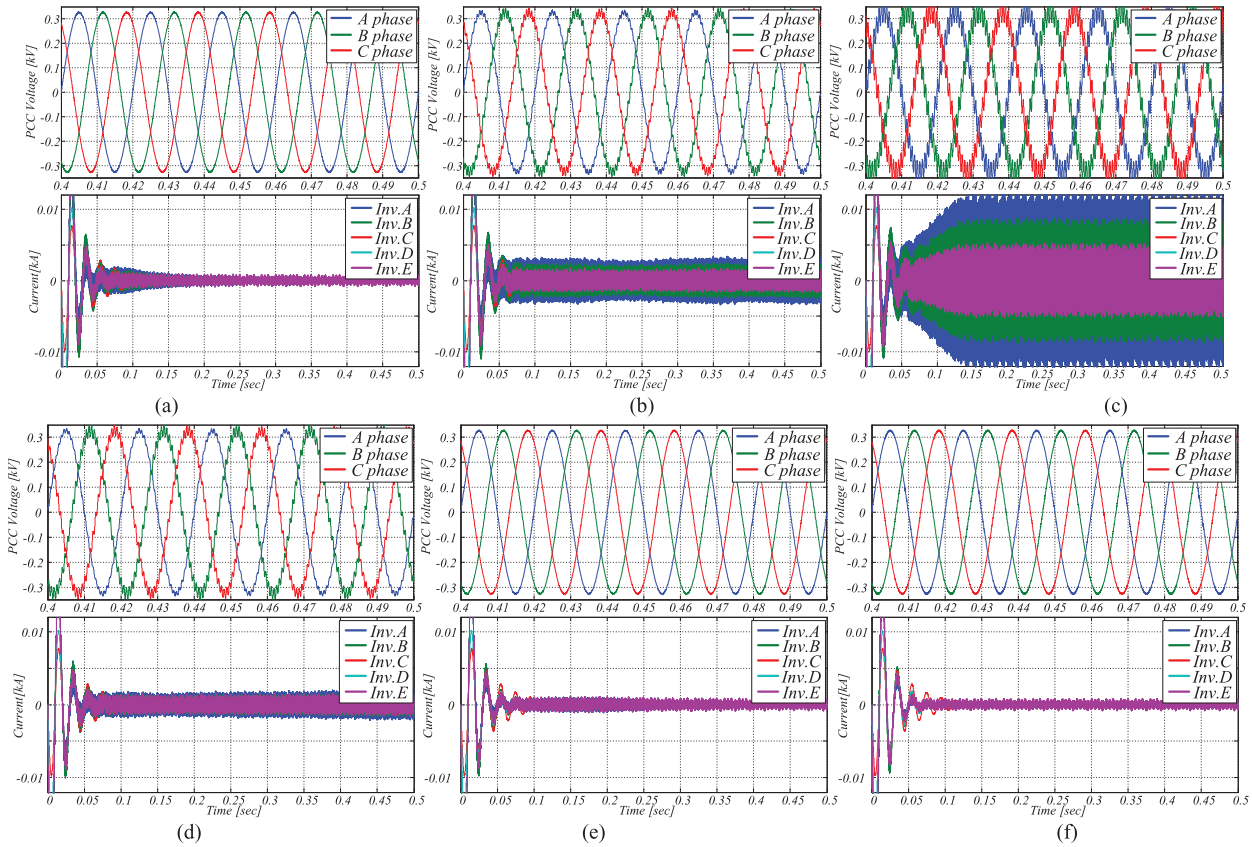

Fig. 12. Time-domain simulation of the test system in Fig. 1 with the different values of L_S at no-load condition, PCC voltage (upper) and inverter currents (lower): (a) 155 uH; (b) 165 uH; (c) 200 uH; (d) 260 uH; (e) 275 uH; (f) 400 uH.

shown in Fig. 12(f). However, when the Nyquist plot moves in the vicinity of $(-1, j0)$ point and does not encircle the point like 155 uH case in Fig. 11, it has a slightly longer time to reach the steady state current as shown in Fig. 12(a) compared to the stable case in Fig. 12(f). When it starts to encircle the $(-1, j0)$ point it becomes unstable as shown in Fig. 12(b). It becomes even worse when it approaches more to the unstable region, e.g. for 200 uH case in Fig. 11 which corresponds to Fig. 12(c). Further, the Nyquist plot reaches another interception point like the 260 uH case. Oscillations in the PCC voltage and the inverter currents are much reduced. If the inductance L_S increases more, the system becomes stable again as shown in the cases from 275 uH to 400 uH.

C. Influence of Inverter Disconnection

Depending on the operating conditions of the inverters in the power system, the load admittance Y_L changes and the stability of the power system is affected. In order to give an example of such stability variations, a stable system with $L_S = 400$ uH, as shown in Fig. 10, is selected as a reference. For this case, the inv. A is selected as the source admittance Y_{SA} as presented in (25). The load admittance Y_{LA} which is seen from the inv. A includes the equivalent admittances of all the other inverters in the power system and the grid admittance. In (26)–(28) some of the inverters are consequently eliminated from Y_{LA} in order to illustrate different operating scenarios, e.g. disconnection of some inverters in the power system. The unstable case at PCC can be found by analyzing the minor loop gain T_{MA} from (31)

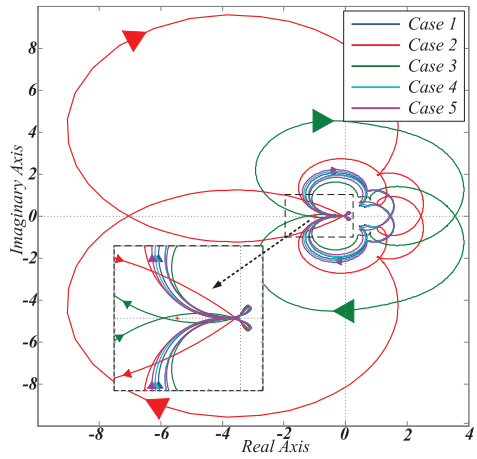

Fig. 13. The Nyquist plot of the minor loop gain T_{MA} for different cases of the load admittances Y_{LA}.

derived for the load admittances expressed in (26)–(30). Fig. 13 shows the estimated stability analysis results from the different minor loop gains.

$$Y_{SA} = Y_{CLA} \tag{25}$$

$$Case\ 1 : Y_{LA} = Y_G + Y_{CPFC} + Y_{CLB} + Y_{CLC} + Y_{CLD} + Y_{CLE} \tag{26}$$

$$Case\ 2 : Y_{LA} = Y_G + Y_{CPFC} + Y_{CLB} + Y_{CLC} + Y_{CLD} \tag{27}$$

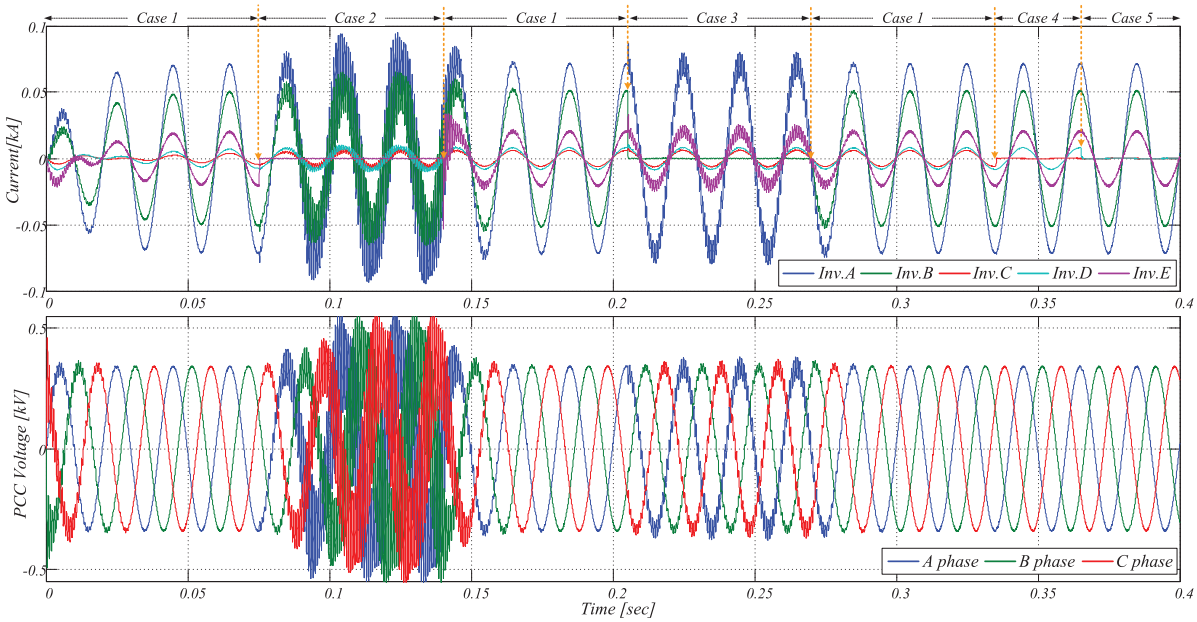

Fig. 14. Time-domain simulation for all cases in Fig. 13 with full load inverter condition: the inverter phase currents (upper) and the PCC voltage (lower).

$$Case\ 3 : Y_{LA} = Y_G + Y_{CPFC} + Y_{CLC} + Y_{CLD} + Y_{CLE} \tag{28}$$

$$Case\ 4 : Y_{LA} = Y_G + Y_{CPFC} + Y_{CLB} + Y_{CLD} + Y_{CLE} \tag{29}$$

$$Case\ 5 : Y_{LA} = Y_G + Y_{CPFC} + Y_{CLB} + Y_{CLE} \tag{30}$$

$$T_{MA} = \frac{Y_{SA}}{Y_{LA}} \tag{31}$$

There are two unstable cases indicated by the encirclement of the $(-1, \text{j}0)$ point, which are Case 2 and Case 3. As interpreted in the previous section, Case 2 is more unstable than Case 3, because the minor loop gain is placed far from the $(-1, \text{j}0)$ point. In order to verify the estimated analysis results in Fig. 13, the time domain analysis is performed. In this time domain simulation, the current references are set to their rated currents. All cases are adjusted by turning on and off the Circuit Breaker (CBs) included in each inverter as depicted in Fig. 9. Therefore, Fig. 14 reflects the exact analysis results obtained from the Nyquist plots in Fig. 13. In Case 1 the system is stable, when all five inverters are connected. However, when inv. B or inv. E are disconnected, the power system becomes unstable as presented in Case 2 and Case 3. The disconnection of the inv. C and inv. D from the power system does not affect the system stability, which corresponds to Case 4 and Case 5. The presented scenarios illustrate some of the unstable / stable conditions of harmonic interactions between multiple inverters and the grid impedance. The instabilities are caused by interactions among the controllers in each inverter, which corresponds to the Nyquist plots in Fig. 13.

Fig. 15. Test platform used for experimental verification.

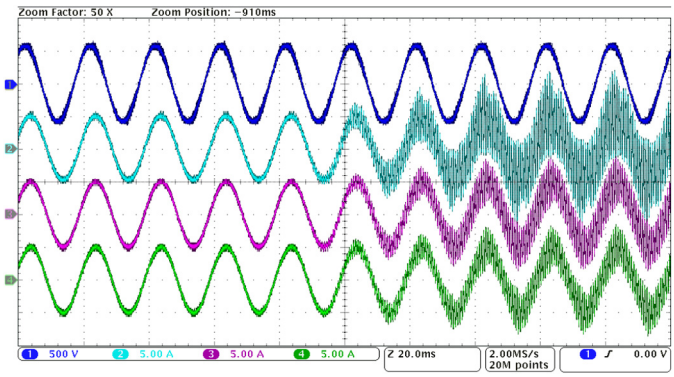

Fig. 16. Phase A time-domain experimental waveform for case 3 with decreased (left half) and designed proportional gain (right half) of the inverter A.

D. Experimental Verification

The setup used for experimental validation is illustrated in Fig. 15 and uses three 5.5 kW Danfoss FC302 inverters, which are controlled through a dSPACE 1007 platform. The filters and control parameters, and the system electrical specifications correspond to Inv. A, Inv. D and Inv. E from Table I except the power rating of the inverters. In Fig. 16, the experimental waveform of the phase A grid voltage (Ch. 1) and phase A currents

of Inv. A (Ch. 2), Inv. D (Ch. 3) and Inv. E (Ch. 4) are shown. To illustrate the stable situation, the proportional gain of Inv. A is reduced to half of its nominal value for the left half of the time window. For the right half of the time window, the proportional gain of Inv. A is reverted to its nominal value leading to harmonic instability as presented in previous analysis and illustrated in Fig. 14.

VI. Conclusion

In this paper, the reason of instability between grid-connected inverters and the passive grid impedance is first explained by using the passivity based approach. With the help of graphical analyzing method, sufficient passive parameter conditions for the stable inverter operation are identified. However, when there are multiple active devices in the AC distribution system, the analysis becomes very difficult to consider all cases. To find out the possible unstable cases among the paralleled inverters, parameter sweeps and different operating conditions are considered, which shows that the harmonic interaction may occur in some conditions. The results show that the possible interaction can happen with multiple grid inverters and grid impedance variations. An analytical model is used to illustrate the harmonic interactions and the PSCAD time domain simulation verified the results. The experimental tests support the simulations and correpsonding analysis.

Acknowledgment

We acknowledge Chang Sung Co. Inc. for providing magnetic materials and inductors for this research.

References

[1] J. H. R. Enslin and P. J. M. Heskes, "Harmonic interaction between a large number of distributed power inverters and the distribution network," *IEEE Trans. Power Electron.*, vol. 19, no. 6, pp. 1586–1593, Nov. 2004.

[2] X. Wang, F. Blaabjerg, and W. Wu, "Modeling and analysis of harmonic stability in an Ac power-electronics-based power system," *IEEE Trans. Power Electron.*, vol. 8993, no. 12, pp. 1–1, Dec. 2014.

[3] "IEEE Recommended Practice and Requirements for Harmonic Control in Electric Power Systems," *IEEE Std 519-2014 (Revision of IEEE Std 519-1992)*. IEEE Standards Association, New York, NY, USA, pp. 1–29, 2014.

[4] R. D. Middlebrook, "Input filter considerations in design and application of switching regulators," in *Proc. IEEE IAS Annu. Meeting*, pp. 366–382, 1976.

[5] J. Sun, "Small-signal methods for AC distributed power systems—a review," *IEEE Trans. Power Electron.*, vol. 24, no. 11, pp. 2545–2554, Nov. 2009.

[6] X. Feng, J. Liu, and F. C. Lee, "Impedance specifications for stable DC distributed power systems," *IEEE Trans. Power Electron.*, vol. 17, no. 2, pp. 157–162, Mar. 2002.

[7] C. Yoon, X. Wang, F. M. F. Da Silva, C. L. Bak, and F. Blaabjerg, "Harmonic stability assessment for multi-paralleled, grid-connected inverters," in *Proc. 2014 Int. Power Electron. Appl. Conf. Expo.*, 2014, pp. 1098–1103.

[8] X. Wang, F. Blaabjerg, M. Liserre, Z. Chen, J. He, and Y. Li, "An active damper for stabilizing power-electronics-based AC systems," *IEEE Trans. Power Electron.*, vol. 29, no. 7, pp. 3318–3329, Jul. 2014.

[9] J. Wyatt, L. Chua, J. Gannett, I. Goknar, and D. Green, "Energy concepts in the state-space theory of nonlinear n-ports: Part I-passivity," *IEEE Trans. Circuits Syst.*, vol. 28, no. 1, pp. 48–61, Jan. 1981.

[10] L. Harnefors, A. G. Yepes, A. Vidal, and J. Doval-Gandoy, "Passivity-based controller design of grid-connected VSCs for prevention of electrical resonance instability," *IEEE Trans. Ind. Electron.*,vol. 62, no. 2, pp. 702–710, Feb. 2015.

[11] S. G. Parker, B. P. McGrath, and D. G. Holmes, "Regions of active damping control for LCL filters," *IEEE Trans. Ind. Appl.*, vol. 50, no. 1, pp. 424–432, Jan. 2014.

[12] V. Blasko and V. Kaura, "A new mathematical model and control of a three-phase AC-DC voltage source converter," *IEEE Trans. Power Electron.*, vol. 12, no. 1, pp. 116–123, Jan. 1997.

[13] C. Bajracharya, M. Molinas, J. A. Suul, and T. M. Undeland, "Understanding of tuning techniques of converter controllers for VSC-HVDC," in *Proc. Nordic Workshop Power Ind. Electron. (NORPIE/2008)*, 2008, p. 8.

[14] G. Raisbeck, "A definition of passive linear networks in terms of time and energy," *J. Appl. Phys.*, vol. 25, no. 12, p. 1510, May 1954.

[15] D. Youla, L. Castriota, and H. Carlin, "Bounded real scattering matrices and the foundations of linear passive network theory," *IRE Trans. Circuit Theory*, vol. 6, no. 1, pp. 102–124, Mar. 1959.

[16] A. Riccobono and E. Santi, "A novel passivity-based stability criterion (PBSC) for switching converter DC distribution systems," in *Proc. IEEE 27th Appl. Power Electron. Conf. Expo.*, pp. 2560–2567, Feb. 2012.

[17] X. Wang, F. Blaabjerg, and P. C. Loh, "Proportional derivative based stabilizing control of paralleled grid converters with cables in renewable power plants," in *Proc. IEEE Energy Convers. Congress Expo. (ECCE'14)*, 2014, pp. 4917–4924.

[18] H. Bai, X. Wang, P. C. Loh, and F. Blaabjerg, "Passivity enhancement of grid-tied converter by series LC-filtered active damper," in *Proc. IEEE 7th Energy Convers. Congress Expo. (ECCE'15)*, 2015.

[19] M. Huang, X. Wang, P. C. Loh, and F. Blaabjerg, "LLCL-filtered grid converter with improved stability and robustness," *IEEE Trans. Power Electron.*, vol. 31, no. 5, pp. 3958–3967, May 2016.

[20] Y. Tang, W. Yao, P. Loh, and F. Blaabjerg, "Design of LCL-filters with LCL resonance frequencies beyond the Nyquist frequency for grid-connected converters," *IEEE J. Emerg. Sel. Topics Power Electron.*, vol. 4, no. 1, pp. 3–14, Mar. 2015.

[21] Cigre Committee SC C6. "Benchmark systems for network integration of renewable and distributed energy resources," Task Force C6.04.02, Technical Brochure 575, 2014.

Changwoo Yoon (S'08) received the B.S. and M.S. degrees from the Department of Control and Instrumentation Engineering, Seoul National University of Technology, Seoul, Korea, in 2007 and 2009, respectively. He is currently pursuing the Ph.D. degree in small-scale power system stability at Aalborg University, Aalborg, Denmark. He was an Engineer with the Advance Drive Technology Co., Anyang, Korea from 2009 to 2013. In 2015, he was a Visiting Scholar with the University of Manitoba, Winnipeg, MB, Canada. His research interests include power electronics for distributed generation, power quality and high power dc–dc converter for renewable energy.

Haofeng Bai (S'15) received the B.Eng. and M. Eng. degree from China University of Mining and Technology, Xuzhou, China, in 2011 and 2014, respectively, both in electrical engineering. He is currently pursuing the Ph.D. degree at Aalborg University, Aalborg, Denmark. His research interests include the control of grid connected converters, power quality improvement, and renewable power generation.

Remus Narcis Beres (S'13) received the M.Sc. degrees in electrical engineering and wind power systems from Transylvania University, Brasov, Romania and Aalborg University, Aalborg, Denmark, in 2012 and 2013, respectively. He is currently pursuing the Ph.D. degree in power filters at Aalborg University. He was with the Distribution Network Operator with Electrica Distribution South Transylvania, from 2010 to 2011. In 2015, he was a Visiting Scholar at Tokyo Metropolitan University, Hachioji, Japan. His research interests include power electronics for distributed generation, power quality, and passive components characterization.

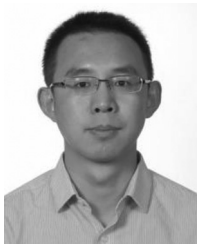

Xiongfei Wang (S'10–M'13) received the B.S. degree from Yanshan University, Qinhuangdao, China, in 2006, the M.S. degree from Harbin Institute of Technology, Harbin, China, in 2008, both in electrical engineering, and the Ph.D. degree from Aalborg University, Aalborg, Denmark, in 2013. Since 2009, he has been with the Aalborg University, where he is currently an Assistant Professor with the Department of Energy Technology. His research interests include modeling and control of grid-connected converters, harmonics analysis and control, passive and active filters, stability of power electronic-based power systems.

He is an Associate Editor of the IEEE TRANSACTIONS ON INDUSTRY APPLICATIONS and serves as the Guest Associate Editor of IEEE JOURNAL OF EMERGING AND SELECTED TOPICS IN POWER ELECTRONICS Special Issue on Harmonic Stability and Mitigation in Power Electronics Based Power Systems and Special Issue on Distributed Generation. He was the recipient of the IEEE Power Electronics Transactions Prize Paper Award in 2014002E

Claus Leth Bak (SM'99) was born in Århus, Denmark, on April 13th, 1965. He received the B.Sc. degree (with Hons.) in electrical power engineering, in 1992 and the M.Sc. degree in electrical power engineering with the Department of Energy Technology (ET), Aalborg University (AAU), Aalborg, Denmark, in 1994. After his studies, he worked as a Professional Engineer with Electric Power Transmission and Substations with specializations within the area of Power System Protection at the NV Net Transmission Company. In 1999, he was employed as an Assistant Professor with ET-AAU, where he holds a Professor position today. He has supervised 15 Ph.D.'s and more than 50 M.Sc. theses. His research interests include corona phenomena on overhead lines, power system modeling and transient simulations, underground cable transmission, power system harmonics, power system protection, and HVDC-VSC offshore transmission networks. He is the author/coauthor of app. 120 publications. He is a member of Cigré C4.502, Cigré SC C4 study committee member, and Danish Cigré National Committee.

Frede Blaabjerg (S'86–M'88–SM'97–F'03) received the Ph.D. degree from Aalborg University, Aalborg, Denmark, in 1992. He was with ABB-Scandia, Randers, Denmark, from 1987 to 1988. He became an Assistant Professor in 1992, an Associate Professor in 1996, and a Full Professor of power electronics and drives in 1998. His research interests include power electronics and its applications such as in wind turbines, PV systems, reliability, harmonics and adjustable speed drives.

He was an Editor-in-Chief of the IEEE TRANSACTIONS ON POWER ELECTRONICS from 2006 to 2012. He was the Distinguished Lecturer for the IEEE Power Electronics Society from 2005 to 2007 and for the IEEE Industry Applications Society from 2010 to 2011. He is nominated in 2014 and 2015 by Thomson Reuters to be between the most 250 cited researchers in Engineering in the world. He was the recipient of 17 IEEE Prize Paper Awards, the IEEE PELS Distinguished Service Award in 2009, the EPE-PEMC Council Award in 2010, the IEEE William E. Newell Power Electronics Award 2014, and the Villum Kann Rasmussen Research Award 2014.